VTT Technical Research Centre of Finland

Mechanistic understanding of the localized corrosion behavior of laser powder bed fused 316L stainless steel in pressurized water reactor primary water

Ge, Yanling; Chang, Litao; Bojinov, Martin; Saario, Timo; Que, Zaiqing

Published in:
Scripta Materialia

DOI:
10.1016/j.scriptamat.2023.115764

Published: 01/01/2024

Document Version
Publisher's final version

Scripta Materialia 238 (2024) 115764

Contents lists available at ScienceDirect

Scripta Materialia

journal homepage: www.journals.elsevier.com/scripta-materialia

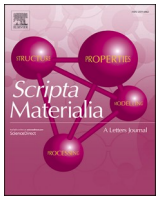

Mechanistic understanding of the localized corrosion behavior of laser powder bed fused 316L stainless steel in pressurized water reactor primary water

Yanling Ge [a,1], Litao Chang [b,1], Martin Bojinov [c], Timo Saario [a], Zaiqing Que [a,*]

[a] Advanced Materials for Nuclear Energy, VTT Technical Research Centre of Finland, Kivimiehentie 3, Espoo 02150, Finland
[b] Shanghai Institute of Applied Physics, Chinese Academy of Sciences, 2019 Jialuo Road, Shanghai 201800, China
[c] Department of Physical Chemistry, University of Chemical Technology and Metallurgy, Kl. Ohridski Boulevard 8, Sofia 1756, Bulgaria

ARTICLE INFO

Keywords:
Laser powder bed fusion
Austenitic stainless steel
Cellular structure
High-temperature water
Localized corrosion

ABSTRACT

The laser powder bed fused (LPBFed) stainless steels showed anomalous and localized corrosion behavior in the nuclear reactor high-temperature water compared to their wrought counterparts, which affects their performance during plant operation. In this study, advanced microstructural characterization was performed on LPBFed 316 L sample along with wrought 316 L sample after corrosion tests to understand the underlying mechanisms. The results showed that an inhomogeneous/discontinuous inner oxide layer formed on LPBFed 316 L, in contrast to the continuous inner oxide layer on the wrought 316 L specimen. This discontinuous inner oxide layer was identified to consist of Cr-enriched nano-sized spinel oxide and the barrier layer features a Ni-enriched hexagonal close-packed Laves phase. Localized/preferential oxidation was found to occur along the cellular walls which were tangled with high density dislocations and decorated with Mn and Si-enriched nano-sized precipitates, and the nano-precipitates were observed in the core of dispersed Cr-enriched inner oxide crystals.

Laser powder bed fusion (LPBF) is an advanced additive manufacturing technique which has the advantage in manufacturing components with complexed geometry [1–9]. LPBF technique has also attracted intensive interests from the nuclear industry, and LPBFed components have been deployed in commercial light water reactors since 2017 [10,11] Most of the components are directly exposed to the high-temperature water during the operation of the reactors, where corrosion of the components can significantly affect the safe operation of nuclear power plants. Therefore, it is critical to understand the corrosion behavior and the underlying mechanisms for the LPFBed materials in the high-temperature water environments.

Few studies have been performed to study the general corrosion and stress corrosion behaviors of the LPBFed stainless steels in the high-temperature water environments [7,8,12–14] Pioneering work by Lou et al. showed the stress corrosion crack growth rate for LPBFed 304 L is higher than the wrought 304 L, and the crack growth rate is highly dependent on the direction that the samples were extracte [7] Recent work by Zhang et al. showed both the as printed and heat treated LPBFed stainless steel had a much higher stress corrosion crack initiation resistance than wrought stainless stee [15] In addition, Song *et al.* showed that LPBFed 316 L also have a much higher resistance to irradiation assisted stress corrosion crack initiation in boiling water reactor high-temperature water environmen [16] Stress corrosion cracking behavior is highly related to static corrosion behavior, the results from the authors in previous studies showed that LPBFed 316 L specimens have a lower corrosion rate in primary water than wrought 316 [17] In addition, it has been found that localized corrosion occurred in the LPBFed 316 L samples heat treated under various schemes [13–15] However, the underlying mechanisms for this phenomenon remain unclear.

In the present study, LPBFed 316 L and nuclear-grade wrought 316 L specimens were exposed to a simulated pressurized water reactor (PWR) primary water and electrochemical impedance spectroscopic (EIS) tests were performed. The morphology, structure and chemistry variation of the oxides formed on the specimens were investigated with nano-scale analytical transmission electron microscopy (TEM). The mechanisms for the unique corrosion behavior of the LPBFed 316 L were proposed based on the complementary analysis.

* Corresponding author.
E-mail address: zaiqing.que@vtt.fi (Z. Que).
[1] First authors

https://doi.org/10.1016/j.scriptamat.2023.115764
Received 24 June 2023; Received in revised form 10 August 2023; Accepted 11 September 2023
Available online 16 September 2023

Table 1
Chemical compositions (wt.%) of the nuclear-grade wrought 316 L material and the LPBF 316 L powder utilized.

	C	N	Si	P	S	Cr	Mn	Ni	Cu	Mo	Fe
Wrought 316L	0.027	0.05	0.37	0.03	0.004	17.3	1.8	11.5	0.024	2.6	Bal.
LPBFed 316 L powder	0.005	0.07	0.25	<0.01	0.005	17.9	1.5	13.0	<0.01	2.7	Bal.

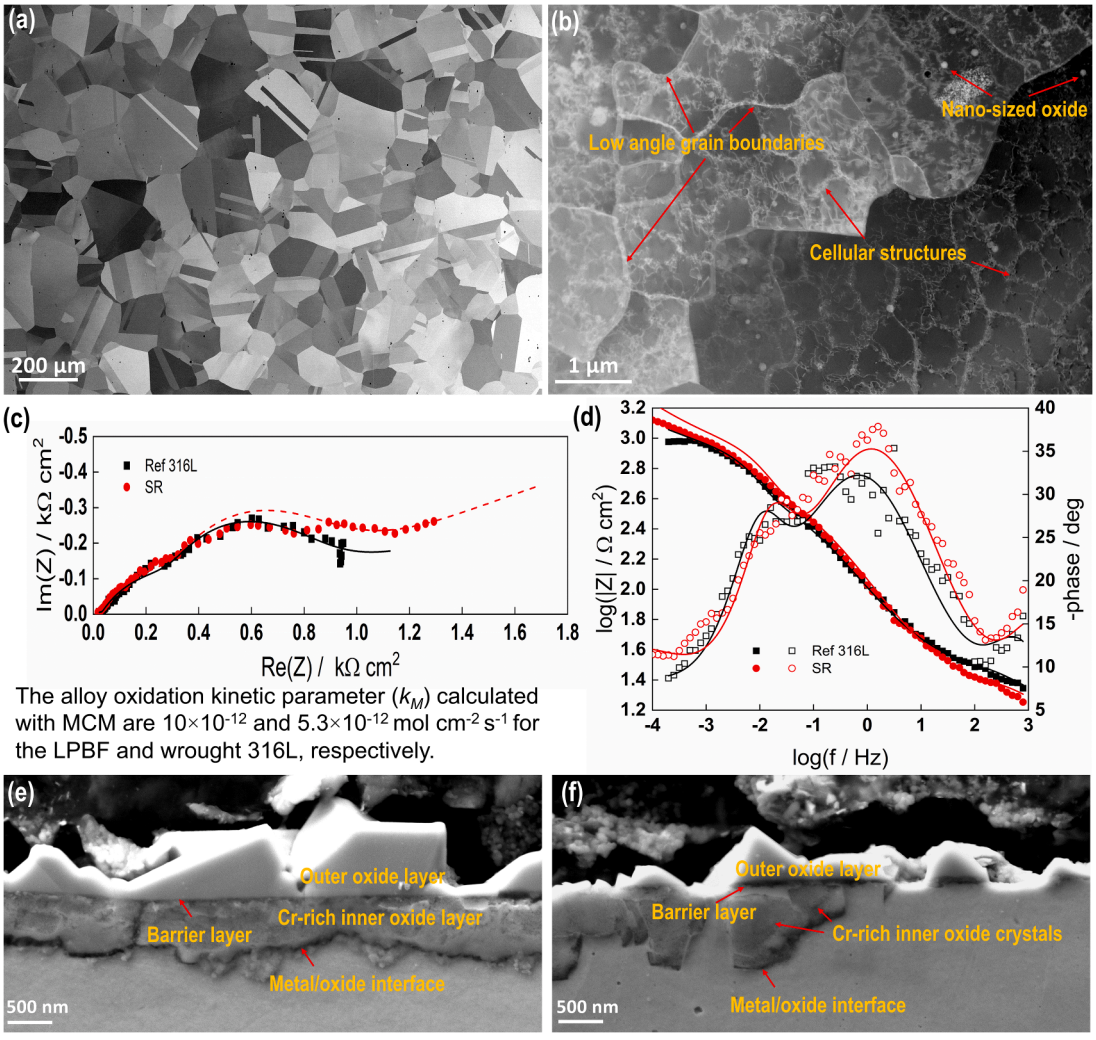

Fig. 1. (a) BSE image of the wrought 316 L; (b) HAADF-STEM image of the LPBFed 316 L, with the nano-sized oxide particles, cellular structures and low-angle grain boundaries arrowed; impedance spectra of the studied materials, presented in (c) complex plane (parameter is frequency in Hz) and (d) Bode coordinates. Points - experimental data, lines - best-fit calculations based on the MCM; Cross sectional images of the oxides on (e) wrought 316 L and (f) LPBF 316 L specimens after EIS measurements in simulated PWR water.

LPBFed 316 L was printed with using an EOS M290 printer using the parameters set of 316L_SurfaceM291 1.1 [17] The compositions of the powder for printing and reference wrought 316 L are shown in Table 1. EIS specimens were extracted in the build direction from the LPBFed block previously stress relieved at 650 °C for 2 h. The dimension of the specimens was 1 × 1 × 0.3 cm^3 and surface was polished using 0.25 µm diamond paste. EIS measurements were performed in simulated start of cycle PWR primary water, i.e., 2.2 ppm Li (added as LiOH), 1000 ppm B (added as H_3BO_3), $pH_{288\ °C}$ 7.0, with 35 cm^3 H_2 / kg H_2O (1.57 mmol kg^{-1} H_2) at 288 °C and 90 bar in a 316 L autoclave attached to a recirculating loop. The measurements were conducted at the open-circuit potential (E_{oc}), using an Ivium CompactStat potentiostat, over a frequency range of 100 kHz to 0.1 mHz, with an alternating current (ac) amplitude of 50 mV (rms). The total exposure time was 2 weeks and the EIS measurement started after one week of exposure.

Electron transparent lamellae for TEM were extracted using focused ion beam (FIB) using a JEOL JIB 4700 microscope. The lamellae were analyzed using a Thermal Fisher Talos F200X analytical TEM with Super-X detector for energy dispersive X-ray spectroscopy (EDS) operated at 200 kV. Bright field (BF) and high-angle annular dark-field (HAADF) Scanning TEM (STEM) images were taken to show the appearance of the oxides, and selected area electron diffraction (SAED) was used to identify structure of the phases. The details of the specimens, autoclave tests, characterization methods and EIS analyses can be found in the Supplement.

The reference nuclear wrought 316 L exhibited a fully recrystallized equiaxed grain structure (average grain size ~110 µm) and extensive annealing twinning (twin fraction ~35 %). In contrast, LPBFed 316 L had a highly textured microstructure in the building direction, and ~70 % of the boundaries were low angle-grain boundaries (2′–10′). Cellular

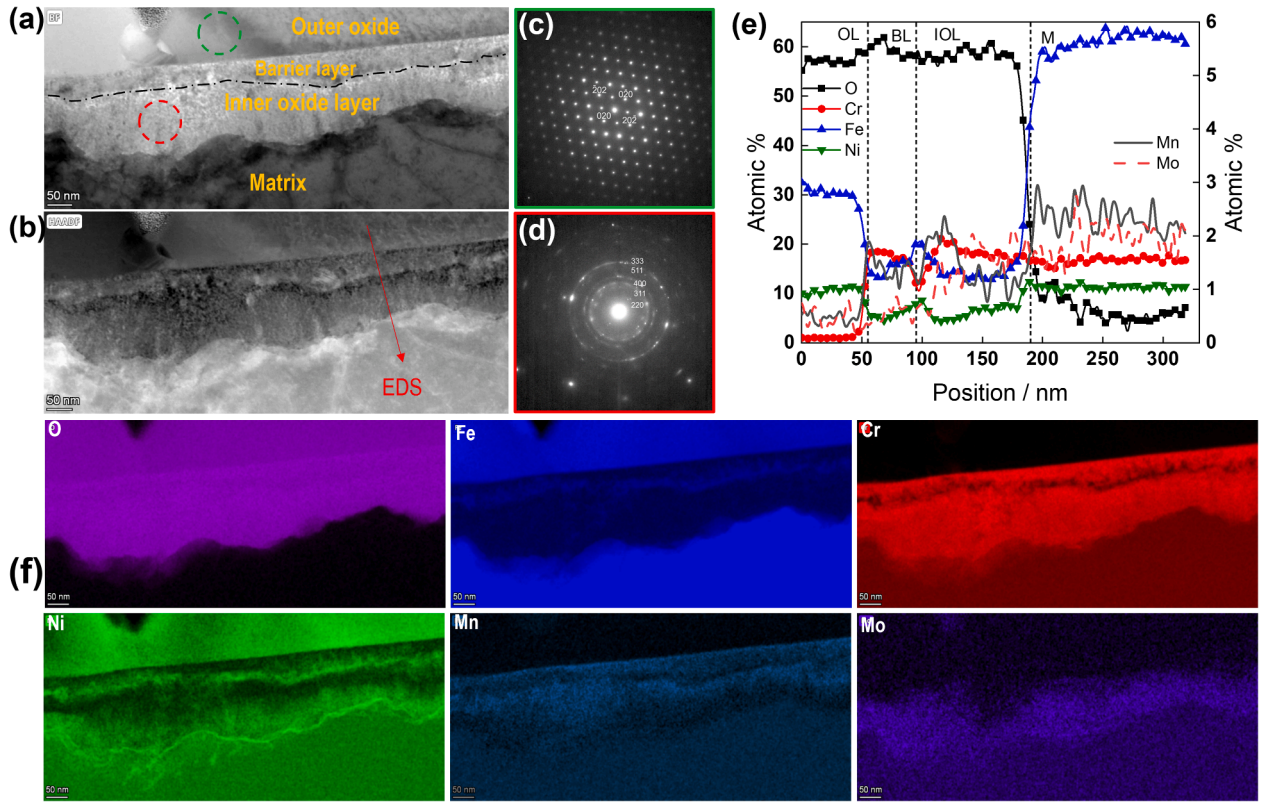

Fig. 2. (a) STEM-BF and (b) HAADF images of oxide layers of the wrought 316 L; (c, d) SAED patterns taken from the outer oxide and inner oxide marked in (a); (e) EDS line profile (at.%) from the marked red arrow in (b); (f) The elemental distribution maps (wt%) of (a, b).

structures with cell size of ~600 nm and high-density dislocations tangled at the cell walls formed within the grains during the printing process. These cell walls were slightly segregated with Cr and Mo and decorated with Mn and Si enriched nano-sized oxide particles. Representative backscattered electron image of the wrought 316 L, and HAADF-STEM image showing the low-angle grain boundaries, cellular structures within the grains and the nano-sized oxide particles are shown in Fig. 1(a, b). EIS data showed that the LPBFed 316 L exhibited a slower corrosion rate than wrought 316 L, as evidenced by a lower impedance magnitude at the low frequency end (Fig. 1(c, d)). The interpretation of the EIS data with Mixed-Conduction Model (MCM [14] reveals that the oxidation rate of LPBFed 316 L at the metal/oxide interface is two times lower than that of the wrought 316 L, indicating lower corrosion release rates and oxide dissolution kinetics of LPBFed 316 L than wrought 316 L. Fig. 1(e, f) show the cross-sectional images of the oxide layers on LPBFed and wrought 316 L samples after EIS measurements. A bilayer structure composed of an inner and an outer oxide layer is formed on both specimens. A thick and uniform inner oxide layer was observed on the wrought 316 L specimen, whilst the inner oxide on LPBFed 316 L was disperse and discontinuous.

Fig. 2(a, b) show the BF-STEM and HAADF-STEM images of the oxide layers on wrought 316 L. The facet-shaped crystals in the outer layer were confirmed to be $NiFe_2O_4$ spinel with a lattice constant close to 8.52 Å *via* SAED, in Fig. 2(c). The inner oxide's ring-shaped SAED fits a spinel ($FeCr_2O_4$) structure with a lattice constant close to 8.51 Å, in Fig. 2(d). The ring pattern indicates that the inner layer comprised of nano-crystals. A well-defined sharp boundary with dislocations entangled in the matrix side was observed at the metal/oxide interface, Fig. 2(a, b). Fig. 2(e) shows the EDS line scan (at.%) from the marked red arrow in Fig. 2(b), which shows fluctuation of chemical composition in both layers. Nevertheless, the outer oxide is a Fe-dominated spinel containing up to 10 at.% Ni, whereas the inner oxide is Cr-dominated containing Fe, Ni, as well as trace amounts of Mo and Mn. The Fe/Ni ratio in the outer oxide is about 4:1 to 7:1, and the Cr/Fe/Ni ratio in the inner oxide layer is around (4 and 5):3:1. The barrier layer between the inner and outer oxides in Fig. 2 featured a segregation line with Cr and Mn depletion as well as Fe and Ni enrichment. The spacing between the segregation line and the interface to outer oxide is in the range from 30 to 55 nm, Fig. 2 (b, e). Elemental segregation is also observed near the metal/oxide interface, where Fe, Ni and Mo exhibited enrichment while Cr and Mn were depleted.

Fig. 3 show the TEM/STEM images of a lamella containing the oxide layers and the LPBFed 316 L matrix, and also the detailed analysis of the oxides. The dislocation cellular structure originating from the LPBF process is visible in the matrix of lamella, as shown in Fig. 3(a, b). The outer oxide crystals are identified to be spinel oxide with lattice constant ~8.50 Å, identical to that formed on wrought 316 L (Fig. 2). The inner oxide layer has a large variation in thickness, from almost zero to 15–30 nm in the thin areas (Fig. 3(e)) to ca. 400 nm in thick areas. Fig. 3(c) shows the thin area of the inner layer and the corresponding SAED patterns from the areas marked by two circles, indicating the smallest selecting area aperture applied. The area framed by the green circle contains both outer and inner oxides and its SAED pattern shows a single orientation. The SAED pattern from the blue circle that contained outer, inner oxide and matrix shows a single orientation from outer layer as well, which suggests that a direct epitaxial relation exists between the oxide layer and the matrix. The epitaxial relationship is further confirmed in Fig. 3(d), which shows a region where the thickness of the inner oxide layer was only around 30 nm as marked with white frame in Fig. 3(c). A ca. 15 nm thick barrier layer could be distinguished from the strong strain field contrast and the faulted lattice. Fast Fourier Transform (FFT) of the barrier area exhibits similar crystal structure and orientation to the outer oxide, which is along zone axis (ZA) [112] of the FCC spinel. The inset with the blue frame illustrates the inner oxide layer and its FFT showed a single orientation similar as the outer oxide, mixed with a weak ring pattern and some amorphous background. The FFT of

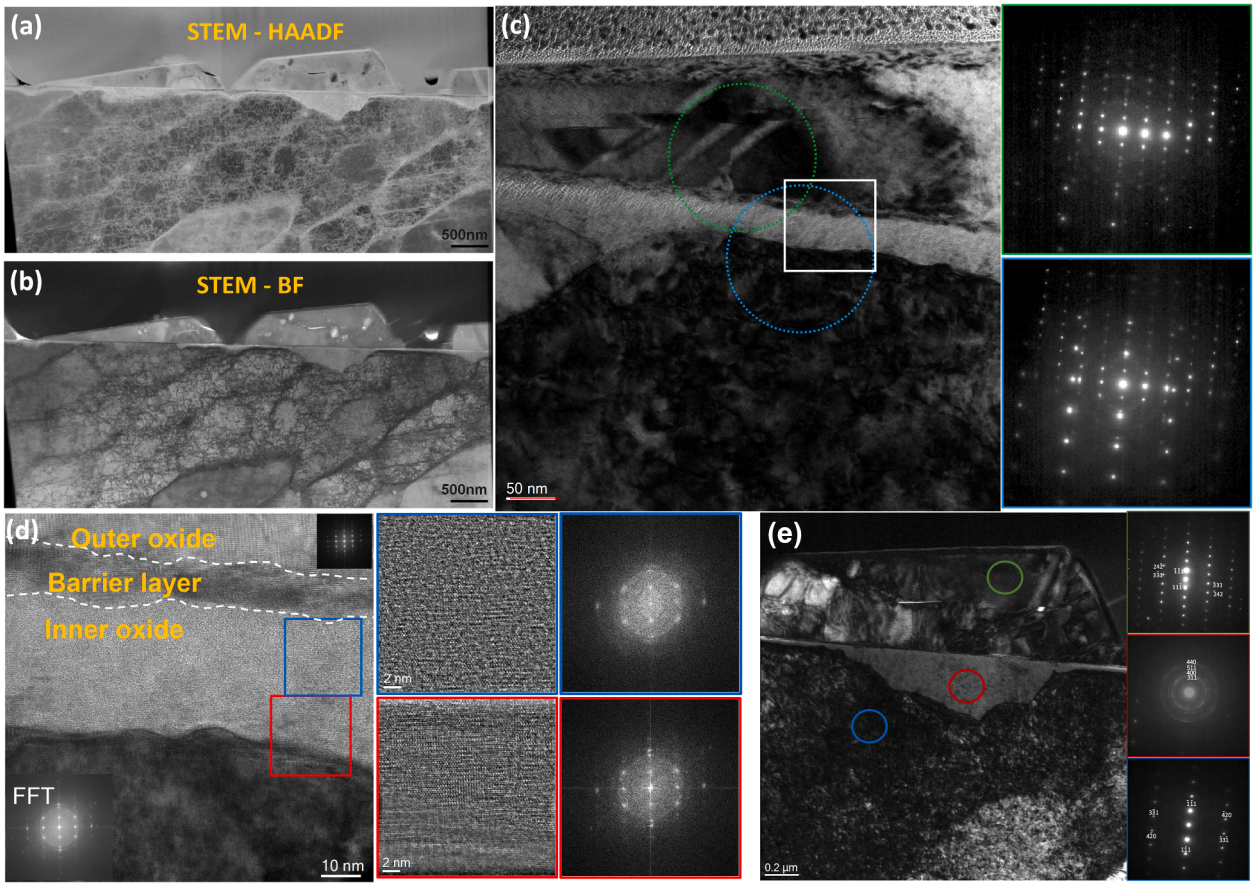

Fig. 3. The morphology of oxides and matrix and their diffraction patterns of the LPBFed 316 L. (a) STEM HAADF and (b) STEM-BF. (c) Thin inner oxide area and the SAED patterns. The patterns in the green circle are from outer oxide and inner oxide while in blue circle from outer oxide, inner oxide and matrix. (d) HRTEM image a thin inner oxide layer region marked with white frame in (c) and two insets from inner oxide and metal/oxide interface, respectively; (e) TEM image of an area with thick inner oxide and SAED patterns from outer oxide (green circle), inner oxide (red circle) and matrix (blue circle), respectively.

the red framed area from the metal/oxide interface indicated some sharp spots from a strong single orientation. The matrix' spots can also be identified from the FFT (bottom left) of the whole image, which was along the ZA [112]. Epitaxial growth between steel matrix and oxide on wrought 316 L was reporte [18]. An epitaxial growth between the inner and outer oxide was observed on LPBFed 316 L for the first time.

Fig. 3(e) illustrates the thick inner oxide area and the SAED patterns from outer oxide, inner oxide and matrix. The SAED patterns from both the matrix and the outer oxide are along the ZA [123] of FCC. The inner oxide nano crystals show a ring pattern. Moreover, HR-TEM image from the thick inner layer region reveals a new phase, which is confirmed with the FFT in Fig. 4(b) of the whole image of Fig. 4(a). The main spots in the FFT belong to the FCC spinel along the ZA [112] whereas the weak spots are identified as Laves phase C14 with hexagonal close-packed (HCP) structure along the ZA [421]. The new phase is aligned with the barrier layer. Four insets revealed the changing crystal structure across the barrier layer. The blue and green framed areas consisted of spinel and Laves phase C14. There was a stacking sequence change in the blue framed area, and new dislocations were formed in the green framed area. The yellow framed area showed a periodic strain field and mixed spinel and Laves phases. In the red framed area, a single Laves C14 phase with HCP structure was detected.

Fig. 5 shows the compositional change in the oxides on the LPBFed sample. The chemistry of outer oxides is identical to that on wrought 316 L, i.e. Fe dominated with slight Ni variation. The inner oxide is Cr-enriched with varying Fe and Ni contents and traces of Mn, the Cr/Fe/Ni ratio ranging from 4:2:1 to 5:3:1. A single Mn- and Cr-rich particle is observed in the core of dispersed Cr-enriched inner oxide crystal. Another two Mn- and Si-enriched particles are observed at the Cr-enriched cell boundaries in the matrix. The chemistry of the inner oxide varies from area to area, especially in the region close to the metal/oxide interface. The enrichment of Cr and Mo at cell boundaries in the matrix is clearly visible, especially for Mo near the metal/oxide interface. Additionally, Cr enrichment can even be observed along previous cell boundaries within the inner oxide crystal as seen in Fig. 5 (b), which apparently originates from the cell boundaries. The growth of inner oxide along the sharp edge to the matrix, the dislocation tangles at the metal/oxide interface and the Mo enrichment all indicate that the metal/oxide interface on the specimen is in coincidence with cell boundaries. These observations suggest that nano-sized oxides and cell boundaries play a critical role during the oxidation of LPBFed 316 L.

A summary of barrier, inner and outer oxide layer thicknesses on stress-relieved LPBF 316 L and reference wrought 316 L specimens is presented in Table 2.

In the present study, an inhomogeneous inner oxide layer with disperse oxide crystals and local variation of thickness was observed on LPBFed 316 L after high-temperature water exposure, in contrast to the uniform inner oxide layer on wrought 316 L. It was found that the corrosion rate of LPBFed 316 L was considerably slower than wrought 316 L. In fact, the lower corrosion rate of LPBFed 316 L in comparison to the wrought 316 L was reported in several previous studies [13,19–22] However, the mechanisms have not been fully elucidated since no direct proof was given.

This paper presents direct evidence of Mn and Cr-rich particles in the core of dispersed Cr-enriched inner oxide crystals on LPBFed 316 L (Fig. 5), which result in a locally increased thickness of the inner oxide

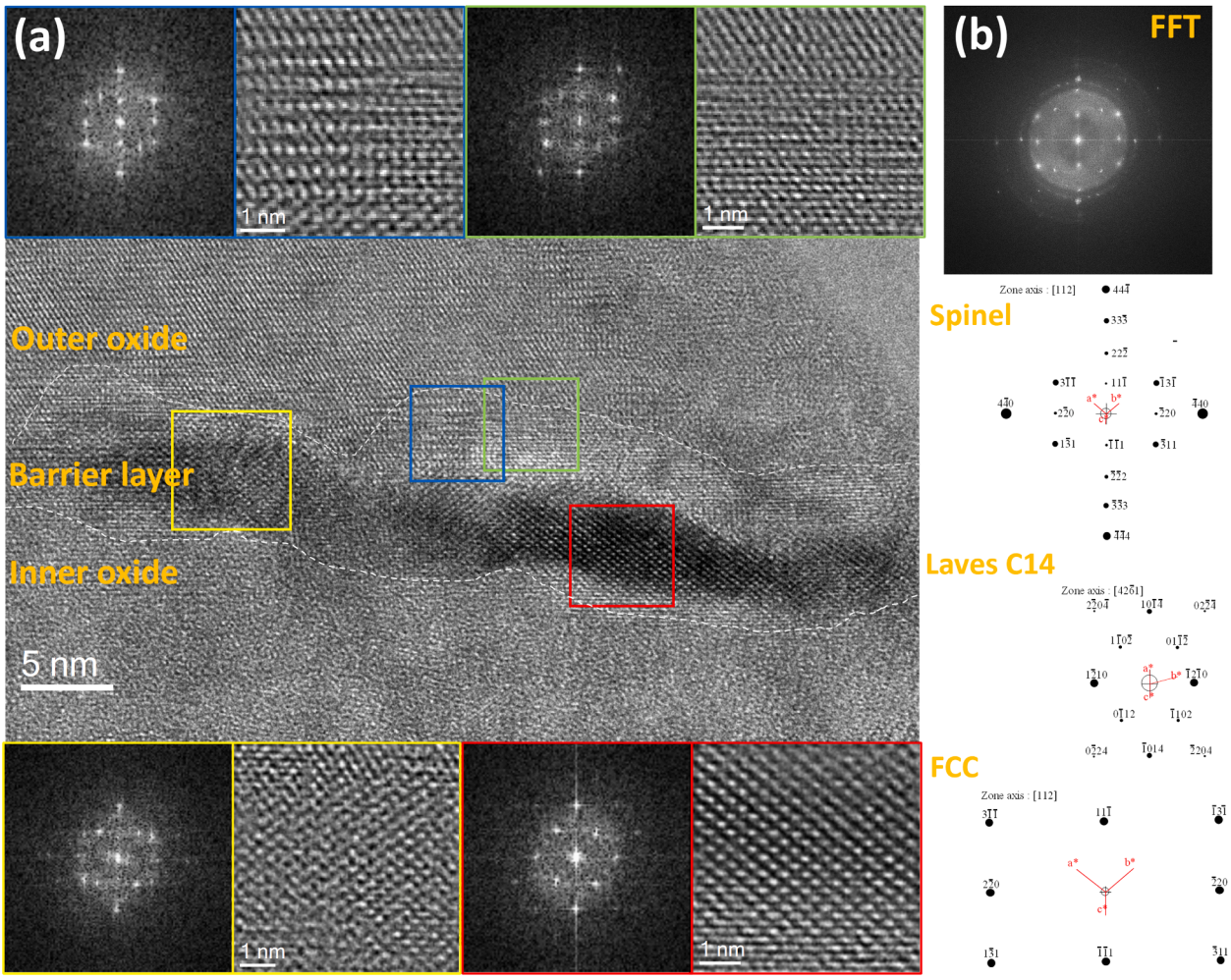

Fig. 4. (a) HRTEM image of thick oxide layers of LPBFed 316 L and insets from different areas in the barrier layer. (b) The FFT from whole image of (a) and schematic simulation of SAED patterns for different phases, i.e. FCC spinel, HCP Laves C14 and FCC matrix.

layer. Upon exposure of LPBFed 316 L to high-temperature water, Cr-enriched inner oxides preferentially nucleate on Mn and Si-rich nano-precipitates near the oxide/water interface. Cathodic processes during passivation partially protect the surrounding areas of nucleation points. This is followed by coarsening of the sparsely distributed Cr-rich oxides enclosing the nano-sized oxides, leading to the formation of an inhomogeneous inner layer. The smaller area fraction of the inner layer at the metal/oxide interface on LPBFed 316 L compared to that on wrought 316 L indicates slower oxide growth kinetics. Subsequently, due to lower supersaturation and re-precipitation, less outer oxide particles are formed at the oxide/water interface on LPBFed than on wrought 316 L. This hypothesis is in line with a recent stud [23] that localized corrosion occurred *via* dissolution of inclusions along cell boundaries at room temperature.

It is worth to note that the barrier layer shows only Ni enrichment on LPBFed 316 L in contrast to Fe and Ni enrichment on wrought 316 L. The HRTEM images confirm the Ni-rich intermetallic phase aligned along barrier layer is Laves phase C14 with HCP lattice. It can be seen from Table 2 that the average thickness of barrier layer, inner oxide layer and outer oxide layer is much smaller on LPBFed 316 L than on wrought 316 L. It could be reasonably assumed that the presence of Laves phase in barrier layer could reduce the corrosion rate due to its oxidation resistance with special geometric alignment observed in the present study. In PWR primary water environment with dissolved hydrogen, Ni in metallic form at the oxide film/solution interface in LPBF 316 catalyzes hydrogen oxidation and limits the Fe dissolution.

The following general conclusions can be drawn from this work: LPBFed 316 L exhibits a much slower corrosion rate than wrought 316 L in PWR primary coolant with dissolved hydrogen at 288 °C. Unlike the uniform inner oxide layer formed on wrought 316 L, LPBFed 316 L displays an inner oxide with Cr-rich inner oxide crystals that are sparsely distributed. A Ni-rich intermetallic phase in the barrier layer on LPBFed 316 L is confirmed to be HCP Laves C14. Direct evidence of nano-precipitates is observed in the core of dispersed Cr-enriched inner oxide crystals on LPBFed 316 L, leading to a locally increased thickness of inner oxide layer and explaining the localized electrochemical activity of the material. In addition to the nano-sized oxides, dislocation cellular structure contributes to that activity. An epitaxial growth

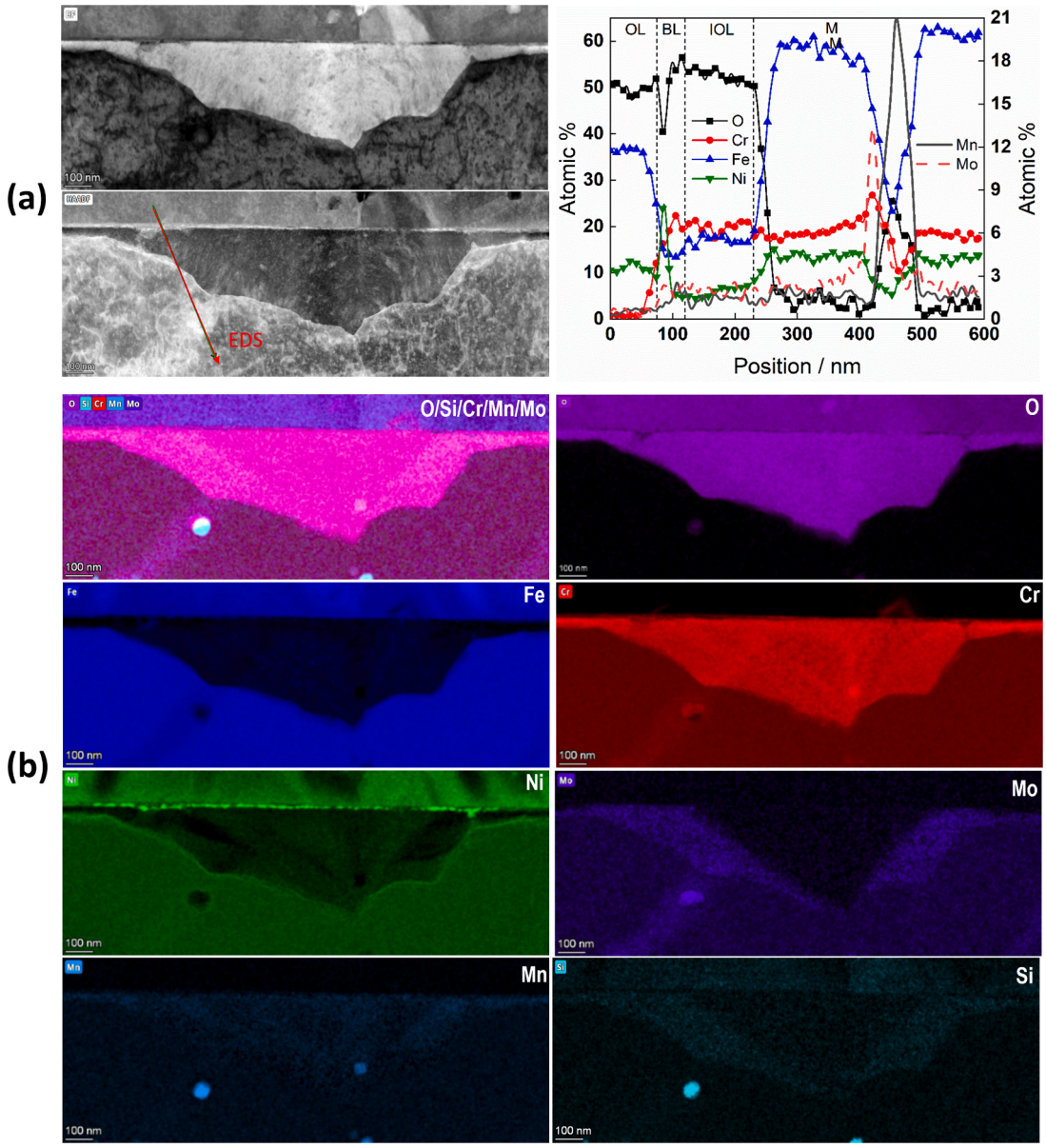

Fig. 5. (a) STEM-BF and STEM-HAADF images of the inner oxide area in LPBFed 316 L lamella and EDS line profile (at%) as marked by the red arrow. (b) The elemental map (wt%) of (a).

Table 2
Summary of the thickness of the barrier layer and the inner and outer oxide layers on the stress-relieved LPBF 316 L and reference wrought 316 L specimens.

Material	Barrier layer	Inner oxide layer	Outer oxide layer
Wrought 316L	Varied with a thickness of 40 ± 15 nm	Uniform with a thickness of 200 ± 80 nm	Uniform with a thickness of 1000 ± 500 nm
Stress relieved LPBF 316L	Varied with a thickness of 15 ± 5 nm	Dispersed with an average thickness of 25 ± 10 nm and locally up to 400 nm	Varied with an average thickness of 400 ± 300 nm

between the inner and outer oxide on the LPBFed 316 L is observed in this work.

Data availability

The data that support the findings of this study are available from the corresponding author upon reasonable request.

Declaration of Competing Interest

The authors declare that they have no known competing financial interests or personal relationships that could have appeared to influence the work reported in this paper.

Acknowledgments

The work is funded by VTT, Shanghai Institute of Applied Physics, Chinese Academy of Sciences (No. E051011031) and Innovation Funding of Shanghai Jiading District (No. E339031031).

Supplementary materials

Supplementary material associated with this article can be found, in the online version, at doi:10.1016/j.scriptamat.2023.115764.

References

[1] H. Springer, C. Baron, A. Szczepaniak, E. Jägle, M. Wilms, A. Weisheit, D. Raabe, Efficient additive manufacturing production of oxide- and nitride-dispersion-strengthened materials through atmospheric reactions in liquid metal deposition, Mater. Des. 111 (2016) 60–69.
[2] G. Wang, H. Ouyang, C. Fan, Q. Guo, Z. Li, W. Yan, Z. Li, The origin of high-density dislocations in additively manufactured metals, Mater. Res. Lett. 8 (8) (2020) 283–290.
[3] D. Kong, C. Dong, S. Wei, X. Ni, L. Zhang, R. Li, L. Wang, C. Man, X. Li, About metastable cellular structure in additively manufactured austenitic stainless steels, Addit. Manuf. 38 (101804) (2021).
[4] T. Ngo, A. Kashani, G. Imbalzano, K. Nguyen, D. Hui, Additive manufacturing (3D printing): a review of materials, methods, applications and challenges, Compos. Part B 143 (2018) 172–196.
[5] Y. Sun, A. Moroz, K. Alrbaey, Sliding wear characteristics and corrosion behaviour of selective laser melted 316L stainless steel, J. Mater. Eng. Perform. 23 (2014) 518–526.
[6] Z. Sun, X. Tan, S. Tor, Selective laser melting of stainless steel 316L with low porosity and high build rates, Mater. Des. 104 (2016) 197–204.
[7] X. Lou, M. Song, P. Emigh, M. Othon, P. Andresen, On the stress corrosion crack growth behaviour in high temperature water of 316L stainless steel made by laser powder bed fusion additive manufacturing, Corros. Sci. 128 (2017) 140–153.
[8] Z. Que, T. Riipinen, S. Goel, A. Revuelta, T. Saario, K. Sipilä, A. Toivonen, SCC behaviour of laser powder bed fused 316L stainless steel in high-temperature water at 288°C, Corros. Sci. 214 (2023), 111022.
[9] S. Choudhary, V. Cruz, A. Pandey, S. Thomas, N. Birbilis, Element-resolved electrochemical analysis of the passivity of additively manufactured stainless steel 316L, Corros. Sci. 189 (2021), 109576.
[10] Westinghouse Creates and Installs Industry's First 3D-Printed Fuel Debris Filter for Nuclear Power Plants, Westinghouse Electric Company, July 2022 [Online]. Available, https://info.westinghousenuclear.com/news/westinghouse-creates-and-installs-industrys-first-3d-printed-fuel-debris-filter-for-nuclear-power-plants?utm_campaign=ogsocial&utm_content=1655125790&utm_medium=social&utm_source=linkedin [Accessed July 2022].
[11] US Department of Energy, 2022. [Online]. Available: https://www.energy.gov/ne/articles/tva-installs-3d-printed-fuel-assembly-brackets-commercial-reactor.
[12] X. Lou, M. Othon, R. Rebak, Corrosion fatigue crack growth of laser additively-manufactured 316L stainless steel in high temperature water, Corros. Sci. 127 (2017) 120–130.
[13] Q. Xiao, J. Chen, H. Lee, C. Jang, K. Jang, Effect of heat treatment on corrosion behaviour of additively manufactured 316L stainless steel in high-temperature water, Corros. Sci. 210 (2023), 110830.
[14] Z. Que, L. Chang, T. Saario, M. Bojinov, Localised electrochemical processes on laser powder bed fused 316L with various heat treatments in high-temperature water, Addit. Manuf. 60 (2022), 103205.
[15] S. Zhang, S. Wang, X. Feng, Z. Ning, J. Hou, W. Kuang, Insights into the stress corrosion cracking resistance of a selective laser melted 304L stainless steel in high-temperature hydrogenated water, Acta Mater. 244 (2023), 118561.
[16] M. Song, M. Wang, X. Lou, R. Rebak, G. Was, Radiation damage and irradiation-assisted stress corrosion cracking of additively manufactured 316L stainless steels, J. Nucl. Mater. 513 (2019) 33–44.
[17] J. Reijonen, R. Björkstrand, T. Riipinen, Z. Que, S. Metsä-Kortelainen, M. Salmi, Cross-testing laser powder bed fusion production machines and powders: variability in mechanical properties of heat-treated 316L stainless steel, Mater. Des. 204 (2021), 109684.
[18] R. Soulas, M. Cheynet, E. Rauch, T. Neisius, L. Legras, C. Domain, Y. Brechet, TEM investigations of the oxide layers formed on a 316L alloy in simulated PWR environment, J. Mater. Sci. 48 (2013) 2861–2871.
[19] R. Revilla, M. Calster, M. Raes, G. Arroud, F. Andreatta, L. Pyl, P. Guillaume, I. Graeve, Microstructure and corrosion behavior of 316L stainless steel prepared using different additive manufacturing methods: a comparative study bringing insights into the impact of microstructure on their passivity, Corros. Sci. 176 (2020), 108914.
[20] R. Revilla, B. Wouters, F. Andreatta, A. Lanzutti, L. Fedrizzi, I. De Graeve, EIS comparative study and critical equivalent electrical circuit (EEC) analysis of the native oxide layer of additive manufactured and wrought 316L stainless steel, Corros. Sci. 167 (2020), 108480.
[21] M. Lodhi, K. Deen, M. Greenlee-Wacker, W. Haider, Additively manufactured 316L stainless steel with improved corrosion resistance and biological response for biomedical applications, Addit. Manuf. 27 (2019) 8–19.
[22] C. Man, C. Dong, T. Liu, D. Kong, D. Wang, X. Li, The enhancement of microstructure on the passive and pitting behaviors of selective laser melting 316L SS in simulated body fluid, Appl. Surf. Sci. 467–468 (2019) 193–205.
[23] M. Tian, J. Choundraj, T. Voisin, Y. Wang, J. Kacher, Discovering the nanoscale origins of localized corrosion in additive manufactured stainless steel 316L by liquid cell transmission electron microscopy, Corros. Sci. 208 (2022), 110659.